The Astrophysical Journal Letters, 979:L32 (6pp), 2025 February 1 https://doi.org/10.3847/2041-8213/ada94f

MUSEQuBES: Unveiling Cosmic Web Filaments at $z \approx 3.6$ through Dual Absorption and Emission Line Analysis

Eshita Banerjee[1], Sowgat Muzahid[1], Joop Schaye[2], Sebastiano Cantalupo[3], and Sean D. Johnson[4]
[1] IUCAA, Post Bag 04, Ganeshkhind, Pune 411007, India; eshitaban18@iucaa.in, sowgat@iucaa.in
[2] Leiden Observatory, Leiden University, P.O. Box 9513, NL-2300 AA Leiden, The Netherlands
[3] Department of Physics, University of Milan Bicocca, Piazza della Scienza 3, I-20126 Milano, Italy
[4] Department of Astronomy, University of Michigan, 1085 S. University, Ann Arbor, MI 48109, USA
Received 2024 November 29; revised 2025 January 6; accepted 2025 January 8; published 2025 January 27

Abstract

According to modern cosmological models, galaxies are embedded within cosmic filaments, which supply a continuous flow of pristine gas, fueling star formation and driving their evolution. However, due to their low density, the direct detection of diffuse gas in cosmic filaments remains elusive. Here, we report the discovery of an extremely metal-poor ($[X/H] \approx -3.7$), low-density ($\log_{10} n_{\rm H}/{\rm cm}^{-3} \approx -4$, corresponding to an overdensity of $\approx$5) partial Lyman limit system (pLLS) at $z \approx 3.577$ along the quasar sightline Q1317–0507, probing cosmic filaments. Additionally, two other low-metallicity ($[X/H] \lesssim -2$) absorption systems are detected at similar redshifts, one of which is also a pLLS. Very Large Telescope (VLT) MUSE observations reveal a significant overdensity of Lyα emitters (LAEs) associated with these absorbers. The spatial distribution of the LAEs strongly suggests the presence of an underlying filamentary structure. This is further supported by the detection of a large Lyα-emitting nebula with a surface brightness of $\geqslant 10^{-19}$ erg cm^{-2} s^{-1} arcsec^{-2}, with a maximum projected linear size of $\approx$260 pkpc extending along the LAEs. This is the first detection of giant Lyα emission tracing cosmic filaments, linked to normal galaxies and likely powered by in situ recombination.

Unified Astronomy Thesaurus concepts: Quasar absorption line spectroscopy (1317); Lyα galaxies (978); Galaxy evolution (594)

1. Introduction

In the current cosmological framework, galaxies emerge within the dense intersections of the cosmic web—a large-scale network of dark matter halos and filaments that span the Universe. These structures channel gas from the intergalactic medium (IGM) into dark matter halos, where it eventually cools, triggering star formation. However, detecting these emissions from the gas in elusive filaments is challenging due to their low densities.

Recent advancements in integral field units with large fields of view, like MUSE (R. Bacon et al. 2010), have revolutionized our ability to detect these filament-like structures, glowing in Lyα emission at high redshifts (M. Fumagalli et al. 2016b; R. Bacon et al. 2021; S. D. Johnson et al. 2022; D. Tornotti et al. 2024a). These observations offer new insights into gas flow from the IGM into galaxies, particularly through "cold-mode accretion" (e.g., D. Kereš et al. 2005), where gas is funneled into galaxies via narrow, dense filaments. This process significantly contributes to the optically thick gas associated with Lyman-limit systems (LLSs: $\log_{10}(N_{\rm H\,I}) > 17.2$; see, M. Fumagalli et al. 2011; F. van de Voort et al. 2012).

M. Fumagalli et al. (2013) have shown that while gas in galaxy halos can account for all LLSs at $z < 3$, at $z \gtrsim 3.5$, the contribution of the IGM to LLSs becomes pronounced, as the overdensities associated with these systems decrease (see, J. Schaye 2001) and the extragalactic UV background (UVB) weakens, enhancing gas shielding. Consequently, LLSs are considered effective tracers of cold-stream inflows onto galaxies, often identified by their low metallicity (e.g., J. Ribaudo et al. 2011; N. H. M. Crighton et al. 2013) or filamentary morphology (e.g., M. Fumagalli et al. 2016b). At $z \approx 3$, only a small fraction (≈18%) of LLSs and partial-LLSs (pLLSs; $16.2 < \log_{10}(N_{\rm H\,I}) < 17.2$) are extremely metal poor, with metallicity being $[X/H] < -3$ (N. Lehner et al. 2016, 2022; E. K. Lofthouse et al. 2023).

Interestingly, in our MUSEQuBES survey, we identified an overdensity of Lyα emitters (LAEs) at $z \approx 3.577$, consisting of seven LAEs arranged in an almost linear configuration. Suspecting a filament connecting these LAEs, we explored potential inflow signatures by modeling absorbers probed by a background quasar and searched for extended emission around this structure. This investigation revealed a low-metallicity absorption system and a coincident giant Lyα nebula. This Letter is organized as follows: Section 2 introduces our data, Section 3 presents absorption measurements and modeling, and finally, we summarize our study and discuss the results in Section 4. We adopt a flat ΛCDM cosmology with $H_0 = 70$ km s^{-1} Mpc^{-1}, $\Omega_M = 0.3$, and $\Omega_\Lambda = 0.7$. Metallicity is expressed as $\log_{10}(Z/Z_\odot) \equiv [X/H]$, where $Z_\odot$ is the solar metallicity (=0.013; see N. Grevesse et al. 2012). Distances are in physical kiloparsecs (hereafter pkpc) unless specified otherwise.

2. Data

The LAE overdensity analyzed in this study is detected toward the quasar Q1317–0507, observed as part of the MUSEQuBES survey (S. Muzahid et al. 2020, 2021; E. Banerjee et al. 2023, 2024). We obtained 10 hr of on-source Very Large Telescope (VLT) MUSE observations with an effective seeing of <0.6. The final data cube has a spatial sampling of $0\farcs2 \times 0\farcs2$

per pixel and a spectral resolution of ≈3600 (FWHM ≈ 86 km s^{-1}) in the optical range (4750–9350 Å). The data reduction process is comprehensively described in S. Muzahid et al. (2021).

Complementary to the MUSE data, we utilized a high-resolution optical spectrum of the quasar from VLT/UVES (R ≈ 45,000), sourced from the SQUAD database (M. T. Murphy et al. 2019). The coadded and continuum-normalized spectrum provides a median signal-to-noise ratio (SNR) of 35 within the Lyα forest region and 80 redward of the quasar's Lyα emission. Additionally, we incorporated near-infrared data from VLT/X-shooter, covering 1000–2480 nm with a spectral resolution of R ≈ 5300 and a median SNR of ≈35. This spectrum, along with its best-fitting continuum, were retrieved from the ESO data archive (S. López et al. 2016).

3. Analysis and Results

S. Muzahid et al. (2020) identified 22 LAEs in the MUSE field centered on the background quasar Q1317–0507 (z_{qso} = 3.7) in the redshift range 2.9 < z < 3.6. These LAEs were detected based on their Lyα emission lines, which typically show offsets of hundreds of km s^{-1} from the systemic redshifts (e.g., C. C. Steidel et al. 2010; O. Rakic et al. 2011; T. Shibuya et al. 2014; A. Verhamme et al. 2018). The Lyα redshifts were corrected using the empirical relation from S. Muzahid et al. (2020). A friends-of-friends algorithm, using a linking velocity[5] of 500 km s^{-1} along the line of sight (LOS), identified a galaxy overdensity with seven LAEs at z ≈ 3.57, making it the most LAE-rich system in the MUSEQuBES sample.

Figure 1 shows the optimally extracted Lyα surface brightness (SB) map of this overdense region (hereafter G7). The redshifts of the seven LAEs range from z ≈ 3.566 to 3.578. The LAE closest to the quasar sightline is Id:2, at a transverse distance of 34 pkpc, followed by Id:3 at 91 pkpc. The other LAEs are located beyond 100 pkpc, with the farthest at 220 pkpc. The redshift histogram reveals that five of the seven LAEs (excluding Id:1 and Id:2) are tightly clustered at z ≈ 3.577, which is ≈8000 km s^{-1} or 20 pMpc from the background quasar.

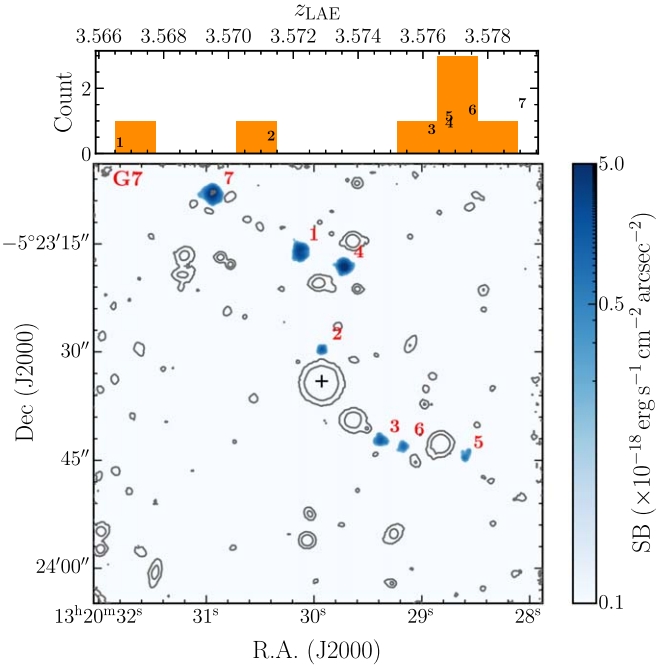

Figure 1. The optimally extracted Lyα SB maps of the seven LAEs (G7) within the MUSE FOV centered on the quasar Q1317–0507 (marked by the "+" sign). The pixels within the 3D segmentation map for each LAE are combined and projected onto the image, with the gray contours representing the 5 and 25σ from the mean flux levels of the continuum-bright objects. A Gaussian smoothing function with σ = 0.″2 (≡ 1 pixel) has been applied to enhance the visual clarity of the SB map. The histogram in the top panel displays the redshift distribution of the LAEs. The object IDs are indicated beside each LAE as well as in the histogram plot.

3.1. Measurements of Absorption Lines Associated with G7

Figure 2 shows the velocity plot for the Lyman-series lines and metal transitions associated with the G7 system. The seven LAEs are marked by red stars, with Δv = 0 corresponding to their median redshift of z = 3.577. To constrain the H I absorber parameters, we simultaneously fitted the Lyman-series lines, from Lyα to H I-λ916, using the Voigt profile fitting software VPFIT (R. F. Carswell & J. K. Webb 2014). This software minimizes χ^2 to determine the best-fitting redshift (z), Doppler parameter (b), and column density (N) of the absorbers. Strong, unfitted absorption in higher-order lines is contamination, as evident from the lack of stronger absorption in Lyα at similar velocities. This underscores the need for simultaneous fitting of all Lyman-series lines. We identified over 30 H I components within ±1000 km s^{-1}, including two pLLSs at −60 and −300 km s^{-1} with H I column densities of $\log_{10}N/\mathrm{cm}^{-2}$ = 16.7 and 16.3, respectively.

[5] Earlier, S. Muzahid et al. (2021) also used a similar velocity window for defining galaxy groups.

Next, we searched for metal transitions associated with G7 within the same velocity range. We detected metal absorption corresponding to H I absorbers at approximately −300, −60, and 300 km s^{-1}, which we labeled as S1, S2, and S3, respectively. The highlighted velocity ranges used to associate aligned transitions were based on the structure of the detected metal absorption lines. C IV absorption was observed in all three systems, while Si IV was detected in S1 and S2. No other metal transitions were detected within this range. For nondetections, we calculated 3σ limiting column densities using the 3σ limiting equivalent width (U. Hellsten et al. 1998), assuming the linear part of the curve of growth.

When fitting the aligned C IV and Si IV transitions, we tied their redshifts. However, the C IV1548 line for S2 and C IV1550 for S1 are contaminated by Mg II absorption from z = 1.52, while C IV1550 in S3 is affected by a z = 2.83 Al III line. To accurately measure the metal absorption parameters, we fitted these contaminating lines as well. The N and b of these blended components are reliably constrained because the corresponding unblended, unsaturated doublet lines provide accurate measurements. We also excluded transitions like C III and Si III due to heavy contamination from the Lyα forest.

Among the metal transitions, we identified four pairs of components (three from S1 and one from S2) where C IV and Si IV are aligned in redshift. By analyzing the b-parameters of these components, we separated the contributions from temperature (T) and turbulent velocity (v_{turb}) in the medium using the relation $b^2 = v_{turb}^2 + \frac{2k_B T}{m_{ion}}$. Here, m_{ion} is

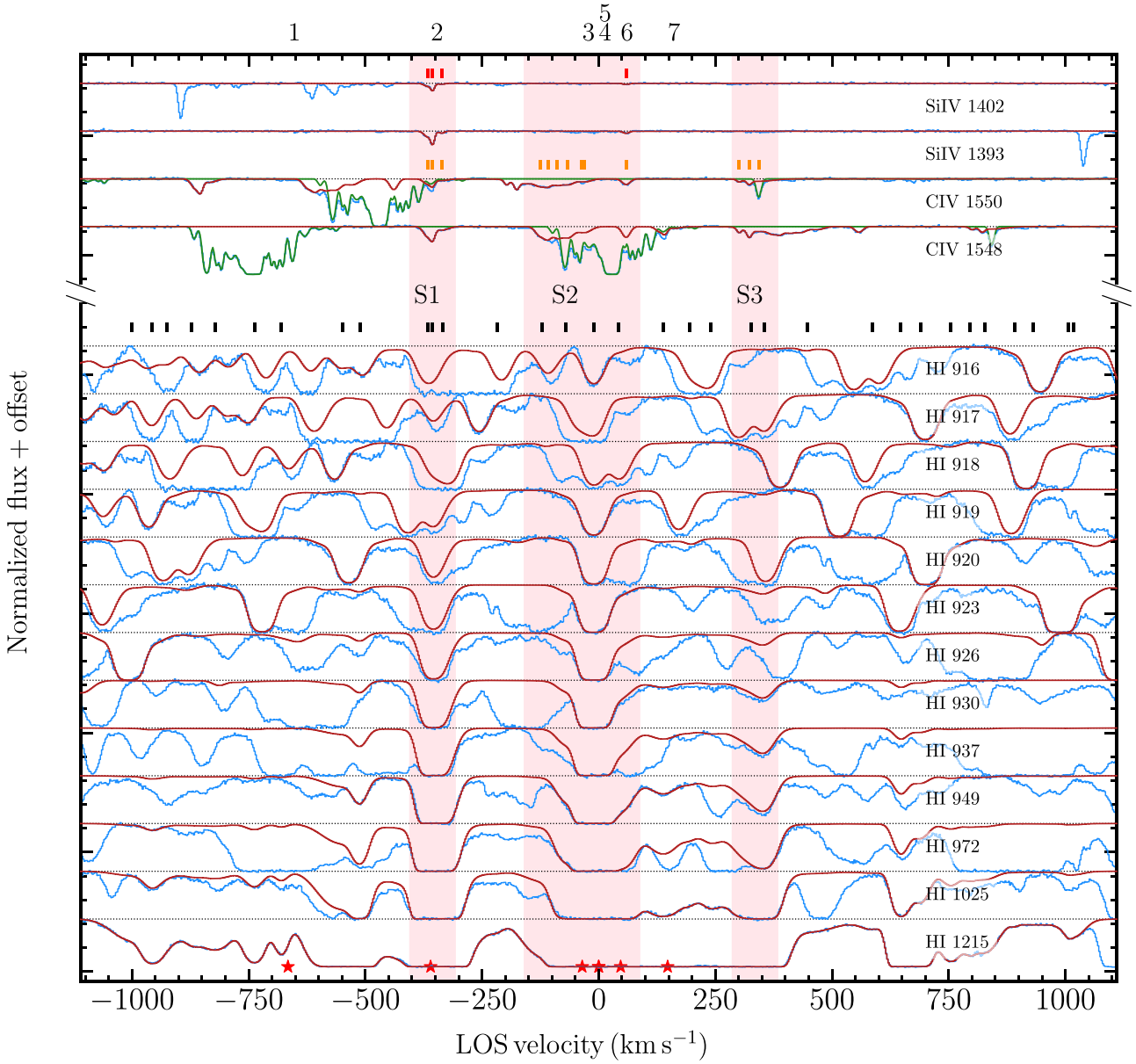

Figure 2. Velocity plot of the G7 system, showing several Lyman-series lines (arranged in descending order of wavelength from bottom to top) along with metal lines detected in the system. The observed spectrum is shown in blue, with the best-fitting model curve from VPFIT in red. Fits for contaminating transitions are displayed in green. The black, orange, and red ticks mark the positions of individual H I, C IV, and Si IV components, respectively. For visual clarity, the normalized fluxes of each line are shifted vertically. The positions of the seven LAEs are marked by red stars at the bottom, and their respective IDs are written on top, with $\Delta v = 0$ corresponding to their median redshift of $z = 3.577$. The total column densities measured within the three pink shaded regions (S1, S2, and S3) are used to construct photoionization models.

the mass of ion, k_B is the Boltzmann constant, and v_{turb} is the turbulent velocity contributing to the nonthermal broadening. The resulting median temperature of the medium is $\log_{10}(T/\mathrm{K}) \approx 4.7 \pm 0.2$. While this method can also be applied using a metal ion and its associated H I absorber, it was not feasible here due to the presence of multiple metal absorption components associated with a single H I absorber.

3.2. Photoionization Model

High-column-density H I absorbers, such as pLLS and LLS, are typically photoionized across redshifts (N. H. M. Crighton et al. 2015; M. Fumagalli et al. 2016b; J. X. Prochaska et al. 2017; N. Lehner et al. 2018, 2022).

Table 1
Range of the Parameters Used for CLOUDY

Parameter	Minimum	Maximum	Interval
$\log_{10} N_{\mathrm{H\,I}}/\mathrm{cm}^{-2}$	12.5	20.5	0.25
z	2.75	4	0.25
$[X/H]$	−4.0	1.0	0.25
$\log_{10} n_H/\mathrm{cm}^{-3}$	−4.5	0.0	0.25

Note. For the Bayesian inference code, we have used interpolation to obtain intermediate values.

We employed CLOUDY (v-C17; G. J. Ferland et al. 2013) to compute ionization corrections, assuming a uniform slab of gas with a constant hydrogen density (n_H) and solar elemental

abundances (M. Asplund et al. 2009) is in thermal and ionization equilibrium. The incident radiation is assumed to be the redshift-dependent UVB given by the F. Haardt & P. Madau (2001; hereafter HM05) model, along with the cosmic microwave background (CMB). It is important to note that for $z > 3$, the UVB models (e.g., HM05; F. Haardt & P. Madau 2012 or V. Khaire & R. Srianand 2019, hereafter KS18) show minimal variation in the relevant energy range. The model iterated until it reached the neutral hydrogen column density ($N_{\rm H\,I}$). We did not include dust or grains, assuming all elements are in the gas phase.

We applied a Bayesian approach to compare the column densities and errors of each ion with a grid of photoionization models to derive the metallicities and densities. This method, commonly used in previous studies (e.g., M. Fumagalli et al. 2011; N. H. M. Crighton et al. 2015; N. Lehner et al. 2018, 2022), is effective in producing robust confidence intervals from posterior probability distributions. We employed likelihood functions similar to M. Fumagalli et al. (2016b). Our model parameters are (i) neutral hydrogen column density ($N_{\rm H\,I}$), (ii) redshift (z), (iii) metallicity ([X/H]), and (iv) the total hydrogen number density (both neutral and ionized), $n_{\rm H} = n_\gamma/U$, where n_γ is the hydrogen ionizing photon density and U is ionization parameter. The parameter ranges are shown in Table 1.

We used the nested sampling Monte Carlo algorithm MLFriends implemented in the `UltraNest`[6] package of Python to obtain the posterior probability density functions (PDFs) of the modeling parameters. Gaussian priors were adopted for $N_{\rm H\,I}$ and z based on VPFIT constraints, while flat priors were used for metallicity and $n_{\rm H}$ across the grid's parameter space.

3.3. Results of Photoionization Modeling

Figure 3 compares the observed column densities with the best-fitting values derived from the medians of the posterior distributions of model parameters for systems S1, S2, and S3.

System S1 is closely aligned in velocity with LAE Id: 2, the galaxy nearest to the quasar sightline. Classified as a pLLS ($\log_{10}N/{\rm cm}^{-2} = 16.3$), it shows C IV and Si IV detections, with upper limits on C II, Si II, Al III, and Mg II. Bayesian analysis with the HM05 (KS18) UVB indicates low metallicity, $[X/H] = -1.98^{+0.14}_{-0.16}$ ($-2.22^{+0.17}_{-0.15}$), and density $\log_{10}\, n_{\rm H}/{\rm cm}^{-3} = -2.65^{+0.11}_{-0.10}$ ($-2.94^{+0.13}_{-0.11}$).

System S2 lies near the redshift of the clustered LAEs and has the highest $\log_{10}N/{\rm cm}^{-2} = 16.7$, also classified as a pLLS. It shows C IV and weak Si IV detections. The metallicity of S2 is extremely low, with $[X/H] = -3.69^{+0.08}_{-0.08}$ (HM05) or $[X/H] = -4.08^{+0.08}_{-0.08}$ (KS18). The density is $\log_{10}\, n_{\rm H}/{\rm cm}^{-3} = -3.95^{+0.2}_{-0.2}$ ($-4.27^{+0.18}_{-0.14}$) for HM05 (KS18).

System S3 has only C IV detected in addition to H I. Hence, instead of using flat priors, a Gaussian prior on density with $\log_{10}\, n_{\rm H}/{\rm cm}^{-3} \approx -3.5 \pm 0.5$, was applied. This corresponds to the maximum C IV ion fraction for the given $N_{\rm H\,I}$ for the metallicities and redshift range included in our grid. This system is also metal poor, with $[X/H] = -2.58^{+0.13}_{-0.07}$ ($-2.94^{+0.16}_{-0.13}$) and $\log_{10}\, n_{\rm H}/{\rm cm}^{-3} = -3.81^{+0.24}_{-0.32}$ ($-4.02^{+0.17}_{-0.27}$) using HM05 (KS18) UVB.

[6] https://johannesbuchner.github.io/UltraNest/

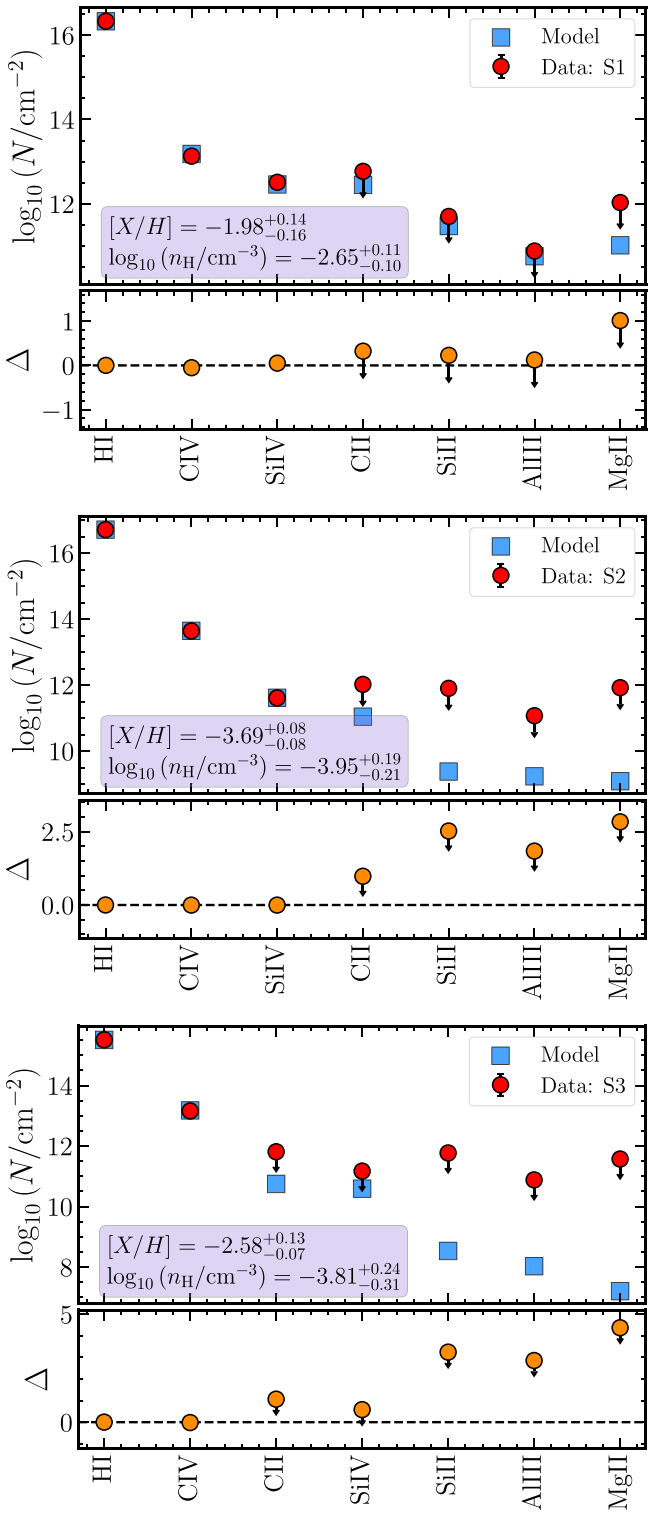

Figure 3. Measured column densities of different transitions associated with S1, S2, and S3 (`top` to `bottom`) are shown in red, with upper limits indicated by downward arrows. Blue squares represent the predicted column densities based on the median values of the model parameters from their respective posterior PDFs. The median values of metallicity and $n_{\rm H}$ along with their 16th–84th percentile ranges are displayed at the top. The bottom panel shows the residuals ($\Delta \equiv \log_{10} N - \log_{10} N_{\rm model}$).

4. Discussion and Conclusion

4.1. The G7 System as a Tracer of Filamentary Structure

To assess the overdensity of the G7 system, we used the LAE luminosity function (LF) to estimate the expected number

of LAEs in a cosmological volume corresponding to that of the G7 system. The LFs of A. B. Drake et al. (2017) and E. C. Herenz et al. (2019) predict only 0.6 and 0.8 LAEs, respectively, with $\log_{10}\ (L_{\mathrm{Ly}\alpha}/\mathrm{erg\ s^{-1}}) \geqslant 41.4$, which is the lowest detected luminosity in the G7 system. Detecting seven LAEs thus corresponds to a Poisson probability of 3×10^{-6} (2×10^{-5} for a mean of 0.8), confirming that this is a highly overdense region.

The projected spatial distribution of G7 member LAEs is notably nonrandom, forming a near-linear structure (see Figure 1). Using a Monte Carlo toy model, we estimated the chance probability of this alignment. By fitting the pixel coordinates of LAEs with a straight line,[7] we measured the maximum perpendicular distance (ϵ) from the line. Randomly placing seven points in the 324×324 spaxel^2 MUSE field of view (FOV), we repeated this process to compute ϵ_i for 1000 realizations. The probability of $\epsilon_i \leqslant \epsilon$ was found to be ≈0.3%, indicating that such alignments are extremely rare.

Five of the seven G7 LAEs (excluding Id: 1 and 2) are clustered in LOS velocity at $z \approx 3.577$, closely matching the velocity ($\Delta v \approx -60$ km s^{-1}) of the extremely metal-poor system S2 ($[X/H] = -3.69$). These LAEs lie at a projected distance of 100–200 pkpc from the quasar sightline. S2, with $\log_{10} n_{\mathrm{H}}/\mathrm{cm}^{-3} = -4.0$ (corresponding to an overdensity of $\delta \approx 5$; J. Schaye 2001), likely originates from cosmic filaments rather than the CGM (e.g., N. H. M. Crighton et al. 2013; M. Fumagalli et al. 2016a, 2016b; R. Mackenzie et al. 2019). We therefore investigated whether there are any traces of extended Lyα emission around this LAE overdensity.

We reanalyzed the MUSE data using CubEx (S. Cantalupo et al. 2019) on the quasar's point-spread function (PSF) and continuum-subtracted cube, focusing on 5535–5600 Å (±2000 km s^{-1} from $z = 3.577$). We searched for sources with >3500 connected voxels with SNR ⩾ 1.8. To enhance sensitivity to low-SB sources, we applied a 4 pixel (0.″8) Gaussian spatial smoothing. This analysis revealed a large extended structure comprising >10,000 connected voxels, with a projected linear size of ≈260 pkpc. We confirmed that the structure spans 16 distinct wavelength layers to ensure the detection is not spurious.

Figure 4 displays the SB map (top) of the detected structure, with the 7 LAEs marked by green squares and (bottom) the SNR map of the same, overlaid on a single wavelength layer associated to the extended emission. The contours in the middle panel highlight the SB level of 10^{-19} erg s^{-1} cm^{-2} arcsec^{-2}, while that on bottom denotes SNR = 2. Although faint, the detection is significant as it aligns closely with the LAE positions. Two LAEs (Ids: 1 and 2) lie directly within the contour, while two others (Ids: 4 and 7) are just outside it. The white dashed and dotted lines drawn on top of the SB map indicate the best-fit linear alignment of the LAEs and their maximum deviation, ϵ. The figure shows excellent correspondence between the extended emission and the filamentary structure traced by the LAEs.

The absence of emission at the quasar's location (marked by the "x") is likely due to enhanced noise from the PSF subtraction. However, this background source allows direct measurement of the filament's n_{H} and U. Bayesian analysis shows $\log_{10} n_{\mathrm{H}}/\mathrm{cm}^{-3}$ ranges between −4.0 and −2.6 (see Section 3.3), corresponding to $\log_{10} U$ of −0.8 to −2.2 (for HM05). LAE Id: 2, located at 34 pkpc of the quasar

[7] Using LinearRegression class from Scikit-learn.

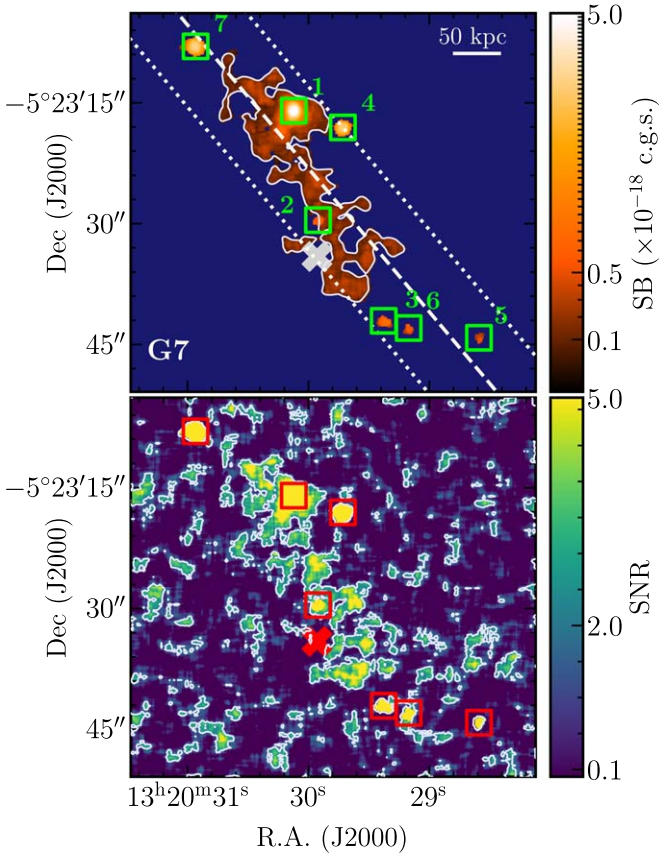

Figure 4. `Top`: the SB profile of the extended filament-like structure as well as the associated LAEs of the G7 system. The contour indicates the SB $=10^{-19}$ erg s^{-1} cm^{-2} arcsec^{-2}. `Bottom`: the SNR map of the extended emission and the associated LAEs, plotted on top of a single wavelength layer associated to the extended emission. The white contours correspond to the SNR of 2. In both panels, the positions of the seven LAEs are highlighted by the squares, while the quasar position is marked by an "x" symbol. The maximum projected length of this structure is ≈260 pkpc. Refer to the text for the details about white dashed and dotted lines.

sightline and ≈300 km s^{-1} along the LOS, could enhance the local radiation field, raising the density estimate by 0.33 ± 0.49 dex (M. Fumagalli et al. 2016b). Even with this correction, n_{H} remains low.

4.2. Origin(s) of the Lyα Nebula Tracing the Cosmic Web

The projected linear size of approximately 260 pkpc classifies this extended emission as "giant" Lyα nebula. Such giant Lyα nebulae are generally detected around high-z quasars (S. Cantalupo et al. 2014; E. Borisova et al. 2016) and between quasar pairs (E. Herwig et al. 2024; D. Tornotti et al. 2024a). However, this is the first detection of a giant Lyα emission tracing cosmic filaments and associated with normal Lyα-emitting galaxies (see D. Tornotti et al. 2024b, for another recent example). Note that none of these LAEs shows He II λ1640 or any other emission line (such as C IV). The low Lyα emission equivalent width (≈50 Å in rest frame) and faint continuum also suggest the lack of AGN activity in these LAEs.

The primary source of this extended Lyα emission might be the "in situ" recombination radiation following photoionization by the UV photons. The Lyα SB expected from an LLS illuminated by the HM05 UVB at $z \approx 3.5$ is 2.2×10^{-20} erg s^{-1} cm^{-2} arcsec^{-2} (see e.g., S. Cantalupo et al. 2005), which is 5 times less than what we detect. Note,

however, that the G7 system is ≈10 times overdense compared to typical regions at this redshift. Consequently, UV photons from the seven LAEs likely contribute significantly to the emission. Their combined SFR, derived from UV continuum flux, is about 4 times higher than expected from the cosmic SFR density at this redshift (P. Madau & M. Dickinson 2014), within their comoving volume. This excess radiation field could explain the observed SB.

Without considering this excess radiation in overdense fields, R. Bacon et al. (2021) proposed that UV-faint galaxies could significantly contribute to the extended Lyα emission. Their Figure 14 suggests that an LF with a slope of $\lesssim -1.8$ integrated down to a Lyα luminosity of 0 or $\approx 10^{37}$ erg s^{-1} can result in an SB of $\approx 10^{-19}$ erg s^{-1} cm^{-2} arcsec^{-2}. Similarly, Y. Guo et al. (2024) proposed that high-z LAEs often have multiple satellite companions that might be the sources of the extended emission $\geqslant$50 pkpc. Although in our case a boost of the UVB by a factor similar to the galaxy overdensity is sufficient to explain the extended emission, we cannot exclude a contribution from fainter galaxies below the detection limit as this depends on the assumptions about the unknown faint end of the LAE LF in such environments. Deeper observations and broader sky coverage with MUSE are essential for uncovering further insights into this intriguing cosmic structure.

Acknowledgments

We thank the anonymous referee for the useful suggestions. We thank Marijke Segers, Lorrie Straka, and Monica Turner for their early contributions to the MUSEQuBES project. E.B. and S.M. thank Raghunathan Srianand, Vikram Khaire and Abhisek Mohapatra for the useful suggestions. This work has used IUCAA HPC facilities. S.C. gratefully acknowledges the support from European Research Council (ERC). E.B., S.M. and S.C. acknowledge the travel fund from the Indo-Italian grant that was helpful for this project. This Letter uses the following software: NumPy (C. R. Harris et al. 2020), SciPy (P. Virtanen et al. 2020), Matplotlib (J. D. Hunter 2007), and AstroPy (Astropy Collaboration et al. 2013).

ORCID iDs

Eshita Banerjee https://orcid.org/0009-0002-7382-3078
Sowgat Muzahid https://orcid.org/0000-0003-3938-8762
Joop Schaye https://orcid.org/0000-0002-0668-5560
Sebastiano Cantalupo https://orcid.org/0000-0001-5804-1428
Sean D. Johnson https://orcid.org/0000-0001-9487-8583

References

Asplund, M., Grevesse, N., Sauval, A. J., & Scott, P. 2009, ARA&A, 47, 481
Astropy Collaboration, Robitaille, T. P., Tollerud, E. J., et al. 2013, A&A, 558, A33
Bacon, R., Accardo, M., Adjali, L., et al. 2010, Proc. SPIE, 7735, 773508
Bacon, R., Mary, D., Garel, T., et al. 2021, A&A, 647, A107
Banerjee, E., Muzahid, S., Schaye, J., Johnson, S. D., & Cantalupo, S. 2023, MNRAS, 524, 5148
Banerjee, E., Muzahid, S., Schaye, J., et al. 2024, arXiv:2411.11959
Borisova, E., Cantalupo, S., Lilly, S. J., et al. 2016, ApJ, 831, 39
Cantalupo, S., Arrigoni-Battaia, F., Prochaska, J. X., Hennawi, J. F., & Madau, P. 2014, Natur, 506, 63
Cantalupo, S., Porciani, C., Lilly, S. J., & Miniati, F. 2005, ApJ, 628, 61
Cantalupo, S., Pezzulli, G., Lilly, S. J., et al. 2019, MNRAS, 483, 5188
Carswell, R. F., & Webb, J. K., 2014 VPFIT: Voigt profile fitting program, Astrophysics Source Code Library, ascl:1408.015
Crighton, N. H. M., Hennawi, J. F., & Prochaska, J. X. 2013, ApJL, 776, L18
Crighton, N. H. M., Hennawi, J. F., Simcoe, R. A., et al. 2015, MNRAS, 446, 18
Drake, A. B., Garel, T., Wisotzki, L., et al. 2017, A&A, 608, A6
Ferland, G. J., Porter, R. L., van Hoof, P. A. M., et al. 2013, RMxAA, 49, 137
Fumagalli, M., Cantalupo, S., Dekel, A., et al. 2016a, MNRAS, 462, 1978
Fumagalli, M., O'Meara, J. M., & Prochaska, J. X. 2016b, MNRAS, 455, 4100
Fumagalli, M., O'Meara, J. M., Prochaska, J. X., & Worseck, G. 2013, ApJ, 775, 78
Fumagalli, M., Prochaska, J. X., Kasen, D., et al. 2011, MNRAS, 418, 1796
Grevesse, N., Asplund, M., Sauval, A. J., & Scott, P. 2012, in ASP Conf. Ser. 462, Progress in Solar/Stellar Physics with Helio- and Asteroseismology, ed. H. Shibahashi, M. Takata, & A. E. Lynas-Gray (San Francisco, CA: ASP), 41
Guo, Y., Bacon, R., Wisotzki, L., et al. 2024, A&A, 688, A37
Haardt, F., & Madau, P. 2001, in Clusters of Galaxies and the High Redshift Universe Observed in X-rays, ed. D. M. Neumann & J. T. V. Tran (Paris: ARISF), 64
Haardt, F., & Madau, P. 2012, ApJ, 746, 125
Harris, C. R., Millman, K. J., van der Walt, S. J., et al. 2020, Natur, 585, 357
Hellsten, U., Hernquist, L., Katz, N., & Weinberg, D. H. 1998, ApJ, 499, 172
Herenz, E. C., Wisotzki, L., Saust, R., et al. 2019, A&A, 621, A107
Herwig, E., Arrigoni Battaia, F., González Lobos, J., et al. 2024, A&A, 691, 210
Hunter, J. D. 2007, CSE, 9, 90
Johnson, S. D., Schaye, J., Walth, G. L., et al. 2022, ApJL, 940, L40
Kereš, D., Katz, N., Weinberg, D. H., & Davé, R. 2005, MNRAS, 363, 2
Khaire, V., & Srianand, R. 2019, MNRAS, 484, 4174
Lehner, N., Kopenhafer, C., O'Meara, J. M., et al. 2022, ApJ, 936, 156
Lehner, N., O'Meara, J. M., Howk, J. C., Prochaska, J. X., & Fumagalli, M. 2016, ApJ, 833, 283
Lehner, N., Wotta, C. B., Howk, J. C., et al. 2018, ApJ, 866, 33
Lofthouse, E. K., Fumagalli, M., Fossati, M., et al. 2023, MNRAS, 518, 305
López, S., D'Odorico, V., Ellison, S. L., et al. 2016, A&A, 594, A91
Mackenzie, R., Fumagalli, M., Theuns, T., et al. 2019, MNRAS, 487, 5070
Madau, P., & Dickinson, M. 2014, ARA&A, 52, 415
Murphy, M. T., Kacprzak, G. G., Savorgnan, G. A. D., & Carswell, R. F. 2019, MNRAS, 482, 3458
Muzahid, S., Schaye, J., Cantalupo, S., et al. 2021, MNRAS, 508, 5612
Muzahid, S., Schaye, J., Marino, R. A., et al. 2020, MNRAS, 496, 1013
Prochaska, J. X., Werk, J. K., Worseck, G., et al. 2017, ApJ, 837, 169
Rakic, O., Schaye, J., Steidel, C. C., & Rudie, G. C. 2011, MNRAS, 414, 3265
Ribaudo, J., Lehner, N., Howk, J. C., et al. 2011, ApJ, 743, 207
Schaye, J. 2001, ApJ, 559, 507
Shibuya, T., Ouchi, M., Nakajima, K., et al. 2014, ApJ, 788, 74
Steidel, C. C., Erb, D. K., Shapley, A. E., et al. 2010, ApJ, 717, 289
Tornotti, D., Fumagalli, M., Fossati, M., et al. 2024a, arXiv:2406.17035
Tornotti, D., Fumagalli, M., Fossati, M., et al. 2024b, arXiv:2412.06895
van de Voort, F., Schaye, J., Altay, G., & Theuns, T. 2012, MNRAS, 421, 2809
Verhamme, A., Garel, T., Ventou, E., et al. 2018, MNRAS, 478, L60
Virtanen, P., Gommers, R., Oliphant, T. E., et al. 2020, NatMe, 17, 261